



High-Velocity Arc Spraying of Fe-based Metallic Glasses with High Si Content

K. Bobzin¹ · W. Wietheger¹ · E. Burbaum¹ · L. M. Johann¹

Submitted: 10 January 2022 / in revised form: 25 May 2022 / Accepted: 14 June 2022
© The Author(s) 2022

Abstract Various feedstocks are available for the thermal spraying of metallic glasses, which are often alloyed with high amounts of cost-intensive elements. In previous steps, a novel, economic Fe-based metallic glass alloy with a high Si content has been developed using melt spinning. The aim of this work is to investigate the application of the alloy using the high-velocity arc spraying (HVAS) process. On this basis, four cored wires are manufactured with the aim of maximizing in situ intermixing and amorphous phase formation during the spraying process. The cross sections of the resulting coatings are analyzed by light microscopy, scanning electron microscopy and Vickers hardness testing. Phase analysis on the coatings is conducted with regards to the formation of amorphous phases using x-ray diffractometry (XRD) and differential scanning calorimetry. The XRD patterns indicate a mixture of (nano-) crystalline ferrite and amorphous phases. In particular, the coating manufactured with wire No. 1, a Fe-B-Si-C-Nb composition, exhibited good intermixing and a highly amorphous structure. This work demonstrates that glassy metallic coatings can be produced by means of HVAS using Fe-based cored wires comprising of conventional filler materials. A successful intermixing, in situ alloying and the subsequent formation of amorphous phases is achieved.

Keywords amorphous phase · cored wire · economical feed material · high-velocity arc spraying · metallic glass

Introduction

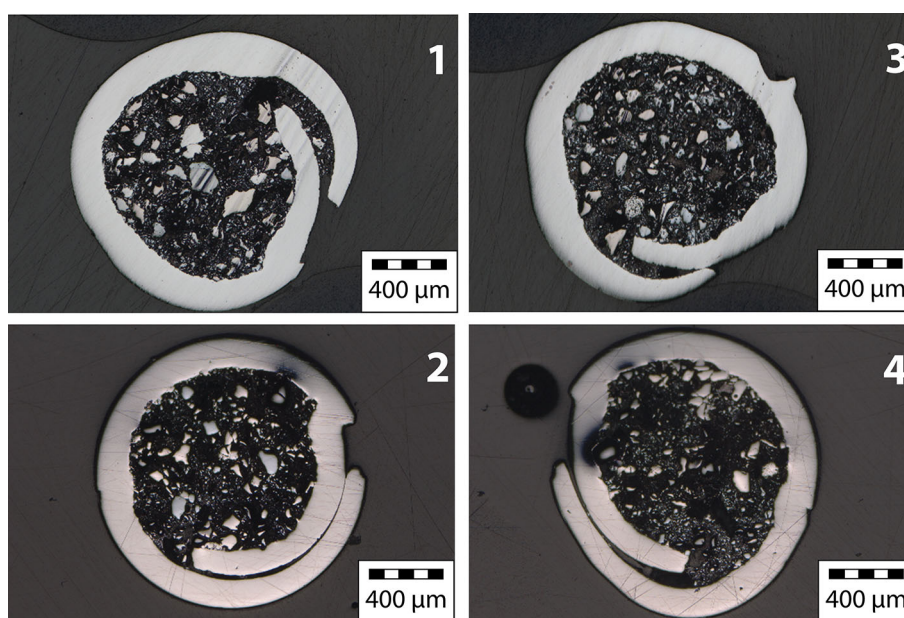
Metallic glasses are alloys which are designed to form amorphous phases. For that, the alloy must be solidified with a cooling rate R above the critical cooling rate R_c or undergo heavy plastic deformation, e.g., by ball milling. Various rules and criterions have been proposed for compositions that achieve a high glass forming ability (GFA). Among those, the Inoue rules are the most popular and practical. Inoue defined the following empirical rules for the estimation of an alloys GFA (Ref 1-3):

1. The alloy should be a multicomponent system comprising of more than three elements.
2. The atomic size ratio among the main constituting elements should be larger than 12%.
3. The constituting elements should exhibit a negative heat of mixing.

Some metallic glasses exhibit a very high GFA and consequently form amorphous phases at cooling rates as low as 10 K/s (Ref 2). However, such alloys are generally far too costly for most applications (e.g., Pd-base) or pose severe manufacturing problems due to high oxidation tendencies (Ti, Zr, Mg-base). Therefore, cost-efficient Fe-based metallic glasses are of great interest for broad industrial applications offering a variety of interesting properties such as high hardness, corrosion resistance and characteristic soft magnetic properties, e.g., extremely low coercive forces, when compared to crystalline alloys (Ref 4-7). However, Fe-based metallic glasses usually require substantially higher critical cooling rates in the magnitude of $10^5 \text{ K/s} < R_c < 10^8 \text{ K/s}$ (Ref 2, 8) to form the desired amorphous phase. The high cooling rates of the process and the possibility to coat dissimilar materials predestine thermal spraying for the manufacturing of metallic glass

✉ L. M. Johann
johann@iot.rwth-aachen.de

¹ Surface Engineering Institute (IOT), RWTH Aachen University, Kackertstr. 15, 52072 Aachen, Germany

Fig. 1 Cross sections of the cored wires**Table 1** Chemical compositions in wt.% according to factory certificates

Wire No.	Fe	B	Si	C	Nb	Mo	Mn
1	bal.	2.0	7.1	1.1	3.7	–	0.2
2	bal.	1.9	6.7	0.7	3.9	–	0.2
3	bal.	1.9	7.0	1.0	3.5	3.6	0.2
4	bal.	1.9	7.1	0.7	3.9	3.3	0.2

coatings. Suryanarayana et al. (Ref 3) have discussed the application of a $\text{Fe}_{50}\text{Cr}_{15}\text{Mo}_{15}\text{C}_{14}\text{B}_6$ amorphous alloy by high-velocity oxygen fuel (HVOF) spraying. In comparison to a hard Cr-coating, the amorphous $\text{Fe}_{50}\text{Cr}_{15}\text{Mo}_{15}\text{C}_{14}\text{B}_6$ layer exceeded the average Vickers hardness as well as the corrosion resistance in an acidic environment. Zhu et al. (Ref 9) reported that the addition of 2 at.% Mo to a Fe-B-Y-Nb metallic glass lead to significantly enhanced GFA, fracture strength and hardness. Previous works (Ref 10) demonstrated that Fe-based amorphous coatings such as Fe-B-Si-Nb-Cr make reasonable thermal barrier coatings, due to the lower thermal conductivity of materials in the amorphous state. The excellent soft magnetic properties of Fe-Cr-B-Si-P and Fe-B-C-P-Si have found coating applications as highly sensitive magnetic sensors, e.g., for the detection of torque, as Suryanarayana and Inoue (Ref 11) point out. Guo et al. (Ref 12) applied Fe-based metallic glass coatings by HVAS using experimental cored wires as a feedstock. The Fe-Cr-B-C-Si-Nb-Mo-Ni coatings exhibited a high content of amorphous phase as well as a high hardness in the range of $950 < \text{HV}_{0.3} < 1,050$. The bonding strength on the AISI 1020 steel reached up to $\sigma_b = 54.8$ MPa and porosities, Φ , were low at $1.9\% < \Phi < 2.2\%$.

Yet the preparation of the cored wire required a separate step of ball milling the granular inner feedstock. Thereby a high densification, homogenization and possibly even formation of amorphous phases was already achieved before spraying. Avoiding such preparation in combination with a low-cost material composition could greatly reduce the overall coating cost. A novel Fe-Si-B-C-Nb-(Mo) metallic glass has been developed in a previous study by melt-spinning trials. The alloy developed comprises of a high Si content as opposed to the common metallic glasses of the Fe-B type, where atomic B-content is highest. Such glasses include Metglas $\text{Fe}_{78}\text{B}_{13}\text{Si}_9$ (Ref 13) or the very popular $\text{Fe}_{72}\text{Si}_4\text{B}_{20}\text{Nb}_4$ (Ref 14, 15).

Experimental Procedure

The experimental procedure consists of the coating application by means of high-velocity arc spraying (HVAS) and a subsequent analysis of coating structure and phase content of the specimen. The sprayed coating specimens are labelled according to the wire number.

Manufacturing of Cored Wires

Cored wires with different compositions are manufactured by Corodur Fülldraht GmbH (Willich, Germany) and Durum Verschleißschutz GmbH (Willich, Germany). The cored wires consist of the sheath, an unalloyed steel, and granular filler material. Sheath and filler material add up to the desired metallic glass composition. All wires are manufactured as seam wires with a diameter of 1.6 mm as shown in Fig. 1. In the cross section, some angular, granular filler material with

diameters of up to 10 μm can be found. Slight loosening of the seams and deformations resulted from the metallographic preparation. All cored wires exhibit a high degree of filler material densification. The chemical compositions as stated in the respective factory certificates (in compliance with (Ref 16) are given in Table 1. Wires No. 1 and 2 as well as No. 3 and 4, respectively, are aiming for similar target coating compositions utilizing different filler material. These different approaches result in slightly varying chemical compositions. The C-content in wires No. 1 and 3 is significantly higher, while wires No. 2 and 4 contain some higher melting carbides, in an attempt to prevent extensive burning losses.

The wires are designed to maximize in situ homogenization to reach the target metallic glass composition in the matrix. A high degree of intermixing and in situ alloying as well as minimal burning losses should achieve a high amount of the desired hard amorphous phase in the HVAS coatings. The addition of 2 at.% Mo in Wires No. 3 and 4. is considered to possibly improve GFA and hardness of the amorphous alloy further, if effects similar to the ones reported by Zhu et al. (Ref 9) can be observed. In that study, an Fe-based metallic glass of metal-metalloid type too has been investigated. A further enhancement of the tribological coating performance would then open up new areas of application.

High-Velocity Arc Spraying

The experimental alloys were sprayed onto AlMgSi1 substrate plates using an HVAS gun specially designed and manufactured by GTV Verschleißschutz GmbH (Luckenbach, Germany). A de Laval nozzle ensures high particle velocities. Nitrogen was used as atomizing gas to reduce melting losses and avoid the formation of solid oxides, which may act as nucleating agents. All wires were sprayed with the spraying parameters, given in Table 2.

The spraying parameters were determined with respect to the literature (Ref 12, 17), prior knowledge of the spray gun and in accordance with DVS 0941-5 (Ref 18). The minimal voltage that guarantees process stability was set at 36 V. After every pass, the specimen were cooled down to $T_{\text{substrate}} < 40\text{ }^{\circ}\text{C}$, which prevents overheating and crystallization during subsequent spraying. With the set parameters, a melting rate of about $\dot{m} \approx 5.3\text{ kg/h}$ is calculated via wire feed and weight per length. The resulting coating specimens No. 1-4 were investigated further.

Porosity and Hardness Measurement

In order to characterize the coatings, the specimens were metallographically prepared. The porosity was measured in 20 light microscopy images at 200 fold magnification using the software (Fiji is Just) ImageJ (Ref 19) in accordance with ASTM E 2109, Method B (Ref 20). The average coating thickness has been measured with five measurements per image. A microhardness tester of type Buehler Micromet 1 by ITW Test & Measurement GmbH (Esslingen am Neckar, Germany) was used for the coating hardness testing. A load of $m = 100\text{ g}$ was applied for an indentation time of $t = 15\text{ s}$. In total, ten measurements per specimen were conducted. The hardness testing is carried out following DIN EN ISO 6507 (Ref 21).

Analysis of Amorphous Phase Content

x-ray diffractometry (XRD) is carried out using a Co- K_{α} radiation source on a Seifert XRD 3000 (GE Energy Germany GmbH, Ratingen, Germany) x-ray diffractometer. Every specimen is measured between $40^{\circ} \leq 2\theta \leq 130^{\circ}$ with an incidence angle of $\omega = 10^{\circ}$. Differential scanning calorimetry (DSC) is applied on detached coating material using a SETSYS Evolution System (Setaram Inc., Lyon, France). For each specimen, two successive measurements are conducted at a heating rate of $\beta = 10\text{ K/min}$ up to $T_{\text{max}} = 820\text{ }^{\circ}\text{C}$. The absence of an exothermic crystallization peak in the second measurement cycle confirms the irreversibility of the reaction and thereby the crystallization.

Results

The results of the coating analysis are presented and discussed. Exemplary light microscopy (LM) and scanning electron microscopy (SEM) images are shown to emphasize features and observations made.

Coating Characterization

The metallographically prepared specimens of the coatings manufactured with the wires listed in Table 1 are investigated by LM, SEM and energy-dispersive x-ray diffractometry (EDX). The cross sections of the coatings

Table 2 Spraying Parameters

Voltage [V]	Wire Feed [m/min]	Scan Velocity [mm/s]	Spraying Distance [mm]	Atomizing gas flow [SLPM]
36	4.20	600	200	2,500

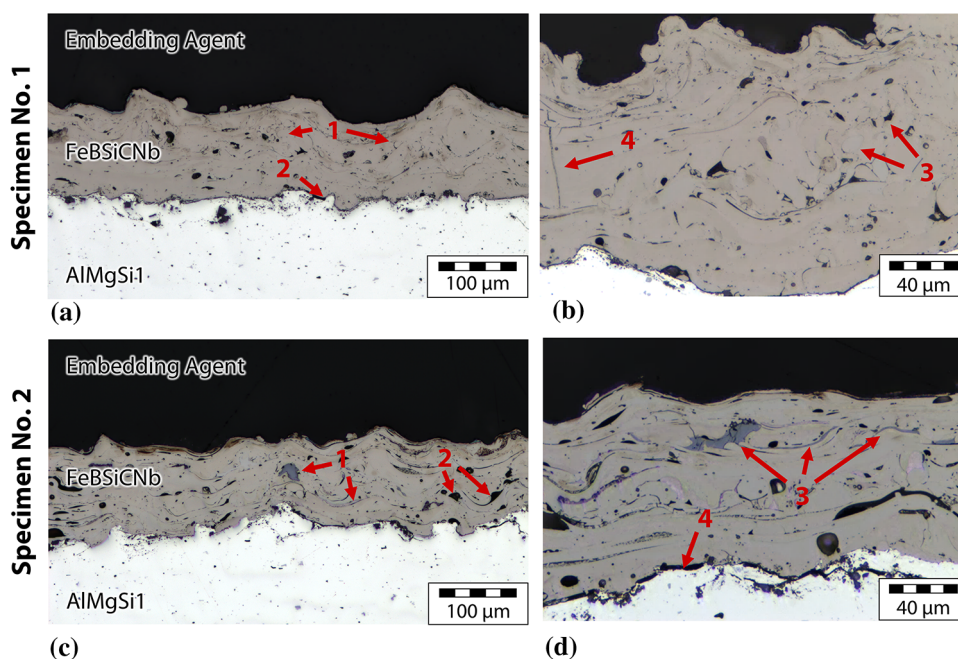
manufactured with wire No. 1 and No. 2 are shown in Fig. 2. A high degree of homogenization of wire sheath and filler material, indicated by the absence of filler material particles or lamellae, is seen in specimen No. 1 (Fig. 2 (a, b)). Markers 1 in Fig. 2 (a) and 3 in Fig. 2 (b) indicate some fine, spherical particles which have been embedded into the coating. These particles are small in diameter and have most likely already solidified in-flight. Some areas with bonding errors are highlighted with marker 2 in (a). These bonding errors occur least frequently in specimen No. 1 among all specimens.

Through 20 images, the porosity was measured to be $\Phi = 3.3^\circ \pm 1.2\%$. Cheng et al. (Ref 17) as well as Guo et al. (Ref 12) reported lower porosities of $\Phi < 2.0\%$ for their respective Fe-based metallic glass alloy. Translamellar cracks as marked (4) in Fig. 2(b) are rarely observed in specimen No. 1. Cracking upon solidification can be attributed to thermal cracking which occurs when molten splats are quenched and contract, releasing quenching stresses (Ref 22). Cheng et al. (Ref 17) also observed free cracking in the bonding region when analyzing a $\text{Fe}_{78.33}\text{B}_{17.95}\text{Si}_{1.64}\text{Nb}_{2.08}$ HVAS coating. The average coating thickness was measured to be $d = 140 \pm 28 \mu\text{m}$, i.e., the coating thickness did vary significantly, although not undercutting $d_{\text{min}} = 100 \mu\text{m}$.

The specimen manufactured with wire No. 2 (Fe-B-Si-C-Nb) exhibits a larger amount of unfused filler material particles and lamellae, when compared to specimen No. 1. These features are denoted in Fig. 2(c) 1 and (d) 3). This can presumably be attributed to the addition of high melting carbides.

Apart from larger dark gray filler material, thinner, highly deformed white particles too, can be distinguished in the cross sections. Hence, some types of the filler material did not intermix adequately. When the homogenization and in situ alloying is insufficient, lamellae may not reach the targeted composition and lack the necessary alloying elements to form amorphous phases under the solidification conditions. Coating defects such as build up pores as denoted in Fig. 2(c) (2) and in (d) bonding errors to the substrate (4) can also be observed. The average coating porosity was determined as $\Phi = 4.5 \pm 4.1\%$. As some of the analyzed coating sections exhibit clusters of build-up voids, the measurement had a high standard deviation of 4.1% and specimen No. 2 had the highest porosity among all specimens. The average coating thickness was measured to be $d = 118 \pm 16 \mu\text{m}$. SEM and EDX (Fig. 3) are used to determine the unfused filler particles denoted (3) in Fig. 2(d). The overview in Fig. 3(a) displays the two major types of filler material lamellae. The previously mentioned thin, white type and a thicker, dark gray type. The EDX analysis of the white lamella on position E1 in the detail image (b) is rich in Nb, $x_{\text{Nb}} > 60 \text{ wt.}\%$, and Fe. Hence, it can be assigned to the filler material ferroniobium. The darker lamella enlarged in the upper detail image of Fig. 3(b) exhibits fine crystalline structures, i.e., an enrichment of a constituting element at the grain boundaries can be observed. The EDX analysis on position E2 indicates a very high Si content of $x_{\text{Si}} \approx 85 \text{ wt.}\%$. Therefore, these filler material particles originate from FeSi feedstock. For coatings which exhibit a higher amount of unfused particles and lamellae, the

Fig 2 Light microscopy of spraying specimen No. 1 at a magnification of (a) 200x and (b) 500x and specimen No. 2 at a magnification of (c) 200x and (d) 500x



powdery filler material in the feedstock should be reassessed toward either smaller fractions or lower melting compositions. A higher densification of filler material in the wire too should improve the melting and intermixing in the arc.

Fig. 4 shows cross sections of the specimens manufactured with wire No. 3 and No. 4, respectively. The cross-sectional analysis of specimen No. 3 in Fig. 4(a) reveals mostly homogeneous lamellae, indicating sufficient intermixing. The coating does however exhibit some defects. Short vertical cracks through single lamellae are marked in Fig. 4(a) 1. Marker 2 highlights a breakout which probably occurred during metallographic preparation. Breakouts are observed when embrittlement and a lack of cohesive bonding occur.

Fig. 4(b) also reveals some small dark gray filler particle (3), which has not been fused into the lamellae. Additionally, some fine white lamellae are identified in other areas of the cross section. A sufficient fusion and intermixing of wire sheath and the different filler materials is essential to reach the target composition and form an amorphous phase. The porosity comprises of build-up pores, including voids and linear detachments (4), which account for the majority, and smaller, spherical gas pores (5). The average porosity of specimen No. 3 was measured at $\Phi \approx 3.2 \pm 1.4\%$. The average coating thickness was calculated to be $d = 137 \pm 25 \mu\text{m}$ for specimen No. 3 and $d = 121 \pm 19 \mu\text{m}$ for specimen No. 4. Here too, a minimal coating thickness of $d_{\text{min}} = 100 \mu\text{m}$ was not undercut. The cross section of specimen No. 4 is presented in

Fig 3 SEM image of specimen No. 2 at 1,000x magnification (a) detailed images at 10,000x magnification and EDX measurement positions (b)

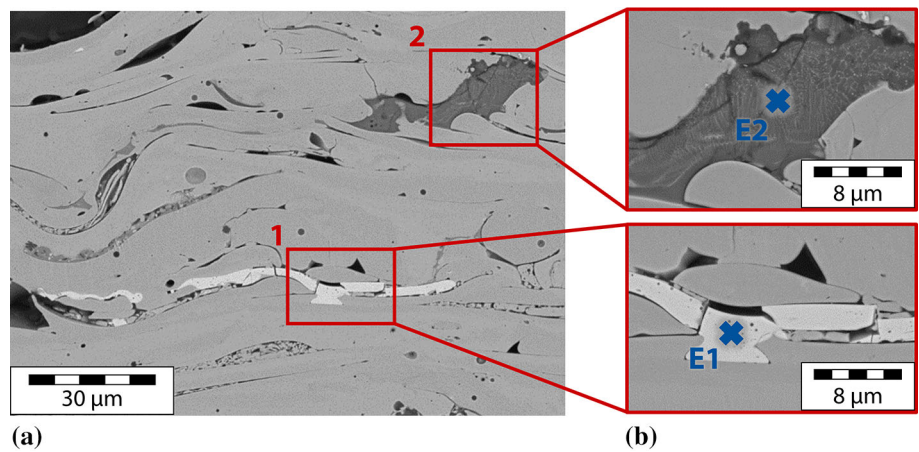


Fig 4 Light microscopy of spraying specimen No. 3 at a magnification of (a) 200x and (b) 1000x and specimen No. 4 at a magnification of (c) 200x and (d) 500x

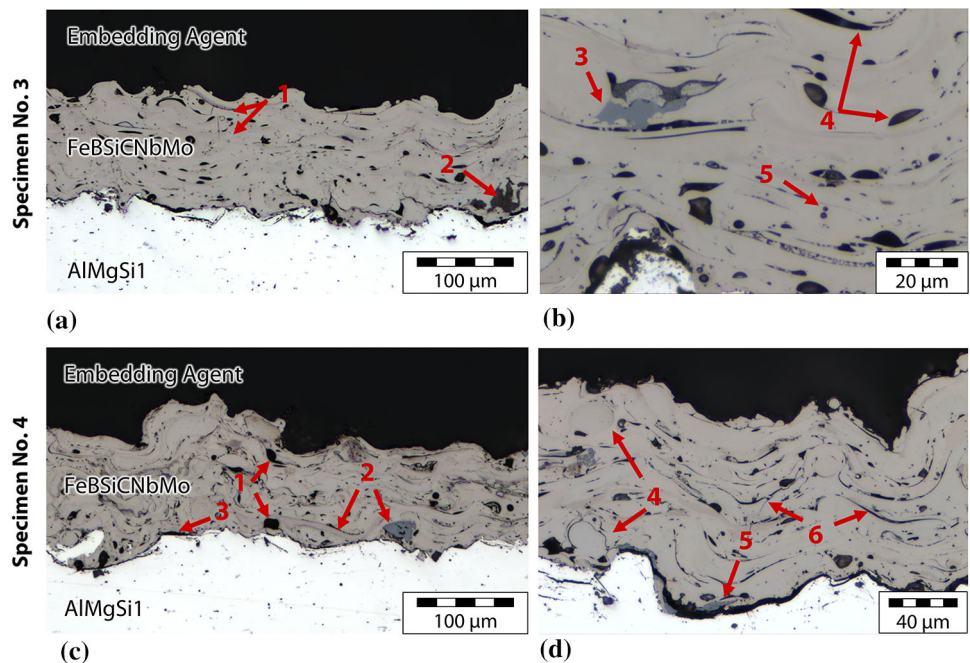


Fig. 4(c) and (d). The porosity follows the already observed distribution with a high amount of voids, as shown by c) 1. In addition to that, a large number of linear detachments can be observed in Fig. 4(6). These features can also be seen in the cross-sectional images provided in the work of Cheng et al. (Ref 17). The average porosity was measured to be $\Phi = 3.3 \pm 1.1\%$. Markings 3 in (c) and 5 in the close up (d) indicate local bonding defects between the coating and the base material. The shape of the detached lamella, which follows the topology of the grid-blasted substrate material, suggests that the local debonding is the result of subsequent splat solidification and thermal residual stresses. The contraction of the quenched lamellae may have led to a pull-out of the cavity. Nevertheless, overall no macroscopic delaminations were detected. Compared with the previous coating, here too, some proportion of non-fused filler particles and lamellae (1, 2) are identified in Fig. 4(c). Analogous to the analysis on specimen No. 2, the filler material residues are investigated by means of SEM and EDX. Within the overview image of the coating manufactured by wire No. 4 in the left of Fig. 5, three different types of distinguishable filler material lamellae are identified. The dark gray lamellae investigated in 1 exhibited a high amount of C and Si of $x_{C,E1} = 41 \text{ at.}\%$ and $x_{Si,E1} = 56 \text{ at.}\%$. Moreover, a very low amount of Fe was detected at E1. Although EDX measurements of elements with small atomic size such as C or B lack precision, it becomes clear that the SiC powder used did not melt into the lamellae. A chemical composition analysis in the spots E2 and E3 revealed a high amount of Mo, $x_{Mo,E2} = 26 \text{ at.}\%$ and $x_{Mo,E3} = 43 \text{ at.}\%$, respectively, as well as C, $x_{C,E2} = 49 \text{ at.}\%$ and C, $x_{C,E3} = 56 \text{ at.}\%$. The Fe content was $x_{Fe} = 19 \text{ at.}\%$ in E2 while no Fe was detected in E3. It

appears that high melting MoC and Mo₂C carbides from the filler material did partially fuse with the sheath to form the lamellae in Fig. 5 2. For the lamellae 3, no such fusing took place and even fine, bright white carbides can be identified. It appears that the high melting carbides could not be fully molten and did not intermix with the remaining compositional elements. The utilization of high melting carbides therefore does not only result in a compositional depletion of the matrix, which may not reach the target glass forming composition, but may also act as nucleating agent. When solid high melting carbides are retained within the molten particles, heterogeneous nucleation on the carbide surface is enabled. These two effects should result in a lower amorphous phase content. These negative effects outweigh possible positive effects in terms of a lowering of melting losses by the mentioned filler material carbides.

X-ray Diffractometry

X-ray diffractometry can be used to examine the crystal structure of a specimen. The formation of broad diffuse “halo peaks” indicates amorphous phases. Diffractograms of the specimen are shown in Fig. 6. The investigations exhibit some correlation with the analysis of the coating structure, especially in regards to intermixing of wire sheath and feedstock. While all specimen display a ferrite peak, specimen No. 1 and especially No. 3 feature a broad underlying halo. This indicates the presences of (nano-) crystalline as well as amorphous phases. Specimen No. 1 was assumed to have the highest degree of homogenization and in situ alloying due to the very low amount of filler material particles found.

Fig 5 SEM image of specimen No. 4 at 1,900x magnification (a) detailed images at 5,000x magnification and EDX measurement positions (b)

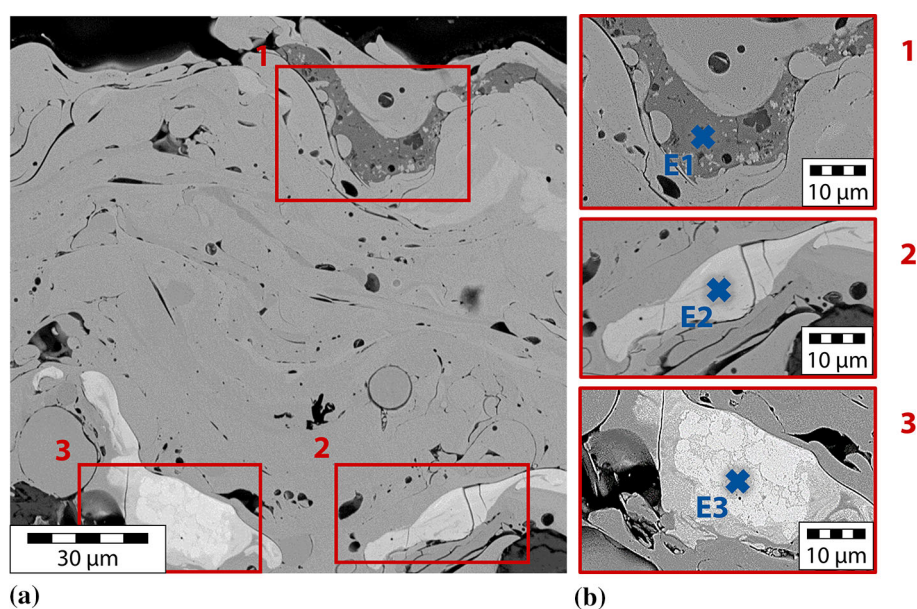
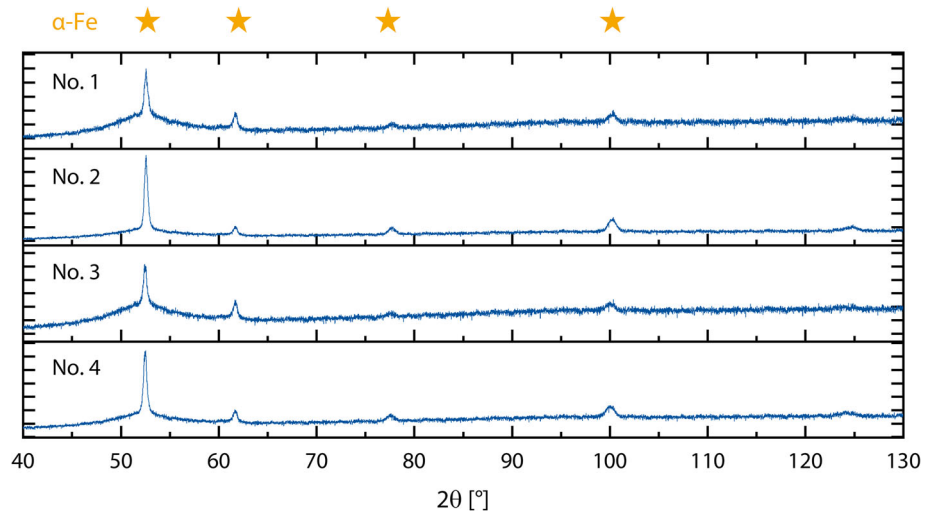


Fig 6 x-ray diffractograms of specimens 1-4

For specimen No. 2, to the contrary, the microstructure analysis suggested a lower degree of intermixing as shown in Fig. 2(c), (d) and Fig. 3. Consequently a predominantly crystalline structure, mostly ferrite matrix, can be identified in the diffractogram. Similarly, specimen No. 3 has formed a larger amount of amorphous phases than specimen No. 4, in which high melting carbides hinder in situ alloying and solidification into the amorphous phase. The XRD analysis therefore supports the hitherto created hypothesis: Insufficient fusing, intermixing and homogenization of the filler material results not only in the entrapment of filler material particles in the coating as revealed in the coating characterization but also the depletion of necessary alloying elements. The depleted lamellae did not reach a metallic glass composition and cannot form amorphous phases.

Differential Scanning Calorimetry

DSC is used to validate the formation of amorphous structures which are indicated by XRD. The exothermal crystallization peaks from the first measurement cycle, which were absent in the second measurement cycle, are plotted in Fig. 7. Figure 7 (a) displays the smoothed heat flow curves as recorded; Fig. 7(b) shows these curves after background subtraction, highlighting the exothermal crystallization peaks. The crystallization temperature T_x , defined as the onset temperature of the crystallization peak, is marked. The glass transition temperature T_g could not be identified from the DSC measurements. The literature suggests that in these cases, especially for Fe-based metallic glasses, T_g may simply be too close to T_x for the small endothermic T_g peak to be observable (Ref 11, 23). The coatings share a similar pattern: Clearly pronounced crystallization peaks as marked. In accordance with the XRD measurements displayed in Fig. 6, the presence of amorphous phases is confirmed for all specimens. The

crystallization enthalpy may be calculated by integrating the crystallization peak area as explained Kong et al. among others (Ref 24). The specific exothermal crystallization enthalpy is highest by far at $h_{\text{cry}} = 61.3 \text{ J/g}$ for specimen No. 1. The amorphous phase content of specimen No. 1 can therefore safely be assumed to be highest.

The curves in Fig. 7(b) reveal that the differences in chemical composition of the cored wires, i.e., addition of Mo appear to influence the crystallization peak position. Differences in T_x with respect to the chemical compositions too can be noticed in Fig. 7(b). While the basic compositions of specimens No. 1 and 2 exhibit a crystallization temperature of $T_x \approx 850 \text{ K}$, the addition of Mo in No. 3, 4 (Table 1) resulted in a slight increase to $T_x \approx 860 \text{ K}$. The DSC measurements supports the findings in the coating characterization. Insufficient intermixing as for No. 2 results in a lower amount of amorphous phases and small crystallization peaks, whereas a high degree of intermixing led to the highest amorphous phase content in No. 1.

Hardness Measurement

Hardness measurements are carried out as described in Section 2.3, and the results are shown as a boxplot in Fig. 8. In a boxplot, the range between the first quartile, above the 25% lowest values, and the third quartile below the highest 25% of values, termed the interquartile range, are displayed as a bar. The respective median value of the data is plotted as a horizontal line. Maximum and minimum outliers are marked with vertical lines. The average hardness of all specimen except for No. 4 was in the range of $800 \text{ HV0.1} < \text{HV} < 900 \text{ HV0.1}$. These values coincide with the measurements on amorphous ribbons in previous works, e.g., an average of $\text{HV} \approx 900 \text{ HV0.1}$ has been measured on an amorphous ribbon with a composition near

Fig 7 DSC heating curves for specimens No. 1-4 before, (a), and after baseline subtraction with crystallization temperature T_x highlighted (b)

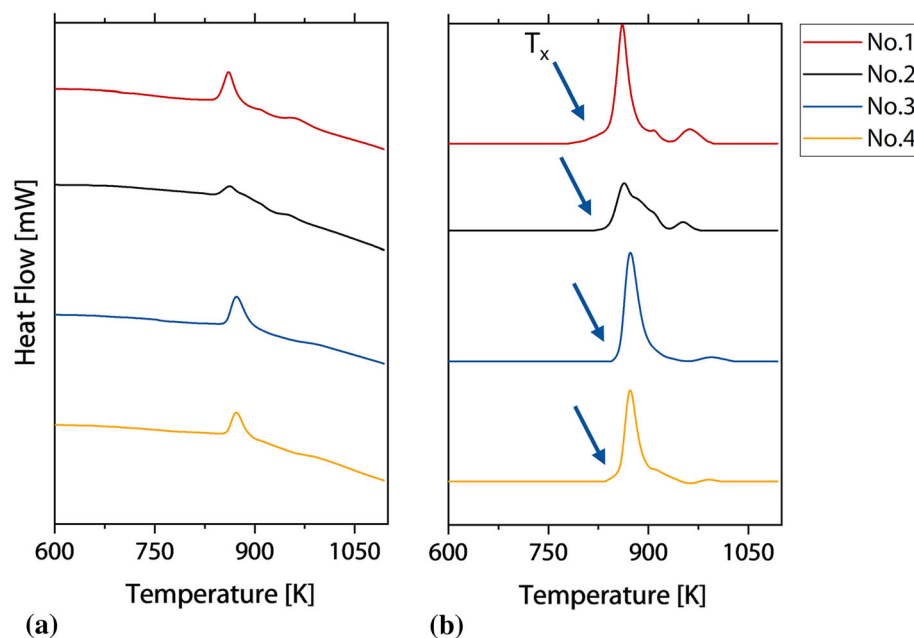
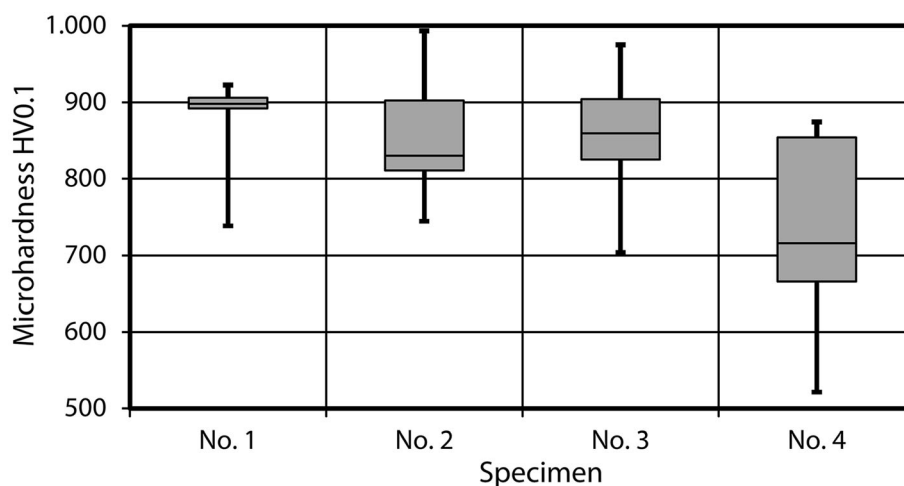


Fig 8 Boxplot of HV0.1 Hardness testing; ten valid indentations per specimen



specimen No. 1 and 2. These hardness values are well within the range of the metallic glass HVAS coating applied by Guo et al. (Ref 12).

The specimen No. 1 does also exhibit not only the highest average hardness but also the least variance. The small width between the quartiles indicates a homogeneous hardness distribution. This may well be attributed to the high degree of intermixing and in situ alloying as suggested by the cross-sectional analysis and the high amorphous phase content revealed by the DSC analysis. In contrast, a large interquartile range with a median value beneath the bar center as observed in specimen No. 4 can be attributed to the more inhomogeneous coating structure. Although artifacts such as unfused filler material particles or lamellae have not been included in the measurement, insufficient homogenization would lead to a local depletion of alloying

elements and inhibit the formation of hard amorphous or nanocrystalline phases. Some formation of borides or silicides as well as solid solution strengthening will however still increase the hardness. The specimens No. 2 and 3 exhibit similarly narrow interquartile ranges and mean values around 850 HV0.1. In contrary to the alloy investigated by (Ref 9), no significant increase in hardness is observed with Mo addition.

Summary and Outlook

Four cored wires were manufactured based on a previously developed novel, cost-efficient Fe-based metallic glass alloy. The cored wires have been sprayed using the HVAS process. Some of the applied coatings exhibit extensive

Table 3 Summary of quantitative investigations conducted

Specimen	No. 1	No. 2	No. 3	No. 4
Porosity [%]	3.3 ± 1.2	4.5 ± 4.1	3.2 ± 1.4	3.2 ± 1.1
Thickness [μm]	140 ± 28	118 ± 16	137 ± 25	121 ± 25
Hardness [HV0.1]	881 ± 55	852 ± 86	838 ± 80	737 ± 117
Specific cryst. enthalpy [J/g]	− 61.3	− 34.3	− 48.9	− 37.4

intermixing, homogenization and a subsequent formation of amorphous phases. Thereby the in situ alloying and manufacturing of glassy coatings by means of cored wires was successful. Some coatings did however exhibit a significant content of unfused filler material, e.g., of carbides or FeSi, FeNb. When the homogenization and in situ alloying was insufficient, as in specimen No. 4, lamellae are depleted of the necessary alloying elements and cannot reach a metallic glass composition, as suggested by the patterns of the XRD analysis. Specimen No. 1 exhibited a broad diffuse halo underlying a ferrite peak. The high amorphous phase content was confirmed by DSC measurements (Fig. 7, Table 3). Specimens of wire No. 1, with a higher carbon content in comparison to wire No. 2, exhibit a larger crystallization peak as well as the highest specific crystallization enthalpy as shown in the summary of the results in Table 3.

Moreover, hardness indentation values deviated far less for specimen No. 1. structural coating defects were least and the average hardness was highest at HV0.1 ≈ 900. Therefore, a higher degree of intermixing, especially the absence of filler material particles or lamellae, results in a maximized amorphous phase content as well as beneficial properties in terms of porosity and hardness. The addition of 2 atm.% Mo did not result in an increase in GFA or hardness.

The next steps in improving coating properties may include:

- Utilization of finer, more narrow fractions of some filler material, e.g., FeNb and FeSi to improve melting behavior and intermixing
- Post-treatments such as laser remelting could enhance the microstructural homogeneity
- Spraying of thicker coatings, depending on application, should yield a higher density of the lower sections of the coating
- Furthermore, the wires will be tested with different thermal spraying processes, e.g., conventional arc spraying (AS) or plasma transferred wire arc spraying (PTWA) for cylinder inner linings.

Acknowledgments The research presented in this work was funded by the German Research Foundation (DFG, Deutsche Forschungsgemeinschaft) within the project BO 1979/67-1 “Fundamental research on deposition of amorphous coatings on surfaces of inner geometries and evaluation of phase stability under tribological loading”. The authors greatly acknowledge the financial support by the DFG. The authors would also like to express their sincere thanks to Corodur Fülldraht GmbH and Durum Verschleißschutz GmbH for manufacturing the experimental cored wires and supporting the aforementioned project.

Funding Open Access funding enabled and organized by Projekt DEAL.

Open Access This article is licensed under a Creative Commons Attribution 4.0 International License, which permits use, sharing, adaptation, distribution and reproduction in any medium or format, as long as you give appropriate credit to the original author(s) and the source, provide a link to the Creative Commons licence, and indicate if changes were made. The images or other third party material in this article are included in the article’s Creative Commons licence, unless indicated otherwise in a credit line to the material. If material is not included in the article’s Creative Commons licence and your intended use is not permitted by statutory regulation or exceeds the permitted use, you will need to obtain permission directly from the copyright holder. To view a copy of this licence, visit <http://creativecommons.org/licenses/by/4.0/>.

References

1. A. Inoue, High Strength Bulk Amorphous Alloys With Low Critical Cooling Rates (Overview), *Mater. Trans. JIM.*, 1995, **36**(7), p 866-875.
2. A. Inoue and K. Hashimoto, *Amorphous and Nanocrystalline Materials: Preparation, Properties, and Applications*, Springer, 2001 Ref (in eng).
3. C. Suryanarayana and A. Inoue, Iron-Based Bulk Metallic Glasses, *Int. Mater. Rev.*, 2013, **58**(3), p 131-166.
4. A. Inoue, B.L. Shen and C.T. Chang, Super-High Strength of Over 4000 Mpa for Fe-Based Bulk Glassy Alloys in [(Fe1–X-cox) 0.75B0.2Si0.05]96Nb4 System, *Acta. Materialia.*, 2004, **52**(14), p 4093-4099.
5. M. Naka, K. Hashimoto and T. Masumoto, Corrosion Behavior of Amorphous and Crystalline Cu50ti50 and Cu50zr50 Alloys, *J. Non-Cryst. Solids*, 1978, **30**(1), p 29-36.

6. A. Makino, C. Chang, T. Kubota and A. Inoue, Soft Magnetic Fe-Si-B-P-C Bulk Metallic Glasses Without any Glass-Forming Metal Elements, *J. Alloy. Compd.*, 2009, **483**(1-2), p 616-619.
7. K. Amiya, A. Urata, N. Nishiyama and A. Inoue, Magnetic Properties of (Fe, Co)-B-Si-Nb Bulk Glassy Alloys With High Glass-Forming Ability, *J. Appl. Phys.*, 2005, **97**(10), p 10F913.
8. B. Cantor, Ed., Rapidly Quenched Metals: Proceedings of the Third International Conference on Rapidly Quenched Metals, organized jointly by the Materials Science Group of the University of Sussex ... held at the University of Sussex, Brighton, on 3 - 7 July 1978, Metals Society, 1978 Ref (in eng).
9. K. Zhu, W. Jiang, J. Wu and B. Zhang, Effect of Mo on Properties of the Industrial Fe-B-Alloy-Derived Fe-Based Bulk Metallic Glasses, *Int J Miner Metall Mater*, 2017, **24**(8), p 926-930.
10. K. Bobzin, M. Öte and T. Königstein, Investigation of Amorphous/Nanocrystalline Iron-Based Thermal Barrier Coatings, *J Therm Spray Tech*, 2017, **26**(3), p 388-397.
11. C. Suryanarayana and A. Inoue, Bulk Metallic Glasses, CRC Press Taylor & Francis Group, 2018.
12. W. Guo, J. Zhang, Y. Wu, S. Hong and Y. Qin, Fabrication and Characterization of Fe-Based Amorphous Coatings Prepared by High-Velocity Arc Spraying, *Mater. Des.*, 2015, **78**, p 118-124.
13. B. Huang, R.J. Perez, P.J. Crawford, A.A. Sharif, S.R. Nutt and E.J. Lavernia, Mechanically Induced Crystallization of Metglas Fe78b13si9 During Cryogenic High Energy Ball Milling, *Nanostruct. Mater.*, 1995, **5**(5), p 545-553.
14. K. Amiya, A. Urata, N. Nishiyama and A. Inoue, Fe-B-Si-Nb Bulk Metallic Glasses With High Strength Above 4000Mpa and Distinct Plastic Elongation, *Mater. Trans. JIM.*, 2004, **45**, p 1214-1218.
15. K. Bobzin, M. Öte, T.F. Linke and T. Königstein, Process Development for Innovative Iron Alloy Metallic Glass Coatings, *Adv. Eng. Mater.*, 2016, **18**(10), p 1833-1840.
16. Deutsches Institut für Normung, Prüfbescheinigungen, 1st ed., Deutsches Institut für Normung, Berlin. Accessed November 19, 2021 Ref (in ger).
17. J.B. Cheng, X.B. Liang, Z.H. Wang and B.S. Xu, Microstructure and Mechanical Properties of Febsinb Metallic Glass Coatings by Twin Wire Arc Spraying, *J. Therm. Spray Tech.*, 2013, **22**(4), p 471-477.
18. Deutscher Verband für Schweißen und verwandte Verfahren e.V., Dvs Merkblatt Dvs 0941-5, 0941-5, Deutscher Verband für Schweißen und verwandte Verfahren e.V., 2012. Accessed December 07, 2021.
19. J. Schindelin, I. Arganda-Carreras, E. Frise, V. Kaynig, M. Longair, T. Pietzsch, S. Preibisch, C. Rueden, S. Saalfeld, B. Schmid, J.-Y. Tinevez, D.J. White, V. Hartenstein, K. Eliceiri, P. Tomancak, and A. Cardona, Fiji: an Open-Source Platform For Biological-Image Analysis, *Nat Methods*, 2012, **9**(7), p 676-682 Ref (in eng).
20. E04 Committee, Test Methods For Determining Area Percentage Porosity in Thermal Sprayed Coatings, 2014th ed., E 2109 - 01, E04 Committee, West Conshohocken, PA. Accessed May 04, 2022.
21. DIN Deutsches Institut für Normung e. V., Metallische Werkstoffe – Härteprüfung Nach Vickers, 6507-1, DIN Deutsches Institut für Normung e. V., Berlin, 2018. Accessed May 04, 2022.
22. P. Fauchais, M. Fukumoto, A. Vardelle and M. Vardelle, Knowledge Concerning Splat Formation: an Invited Review, *J. Therm. Spray Technol.*, 2004, **13**(3), p 337-360.
23. A. Inoue, T. Iwadachi, T. Minemura and T. Masumoto, Nonequilibrium Phases in Fe-X-C (X=Cr, Mo or W) Ternary Alloys Quenched Rapidly from Melts, *Trans. JIM*, 1981, **22**(3), p 197-209.
24. Y. Kong and J.N. Hay, The Enthalpy of Fusion and Degree of Crystallinity of Polymers As Measured By Dsc, *Eur. Polymer J.*, 2003, **39**(8), p 1721-1727.

Publisher's Note Springer Nature remains neutral with regard to jurisdictional claims in published maps and institutional affiliations.